Physical and Control System Design Challenges in Large Range Nanopositioning

Shorya Awtar, Gaurav Parmar

University of Michigan, Ann Arbor, MI 48109 USA
(E-mails: awtar@umich.edu, parmar@umich.edu)

Abstract: There is an increasing need for compact desktop-size nanopositioning systems that can provide motion range of the order of several millimeters and yet achieve nanometric precision, resolution, and accuracy. In this paper, we highlight the several challenges that exist in the physical and control system design of a multi-axis flexure-based XY nanopositioning system capable of large dynamic range (~10^7). There are practical limitations associated with the individual physical components (flexure bearing, actuators, sensors, drivers, and microcontroller) as well as their integration. Once these physical system design challenges are overcome, the ensuing control system design challenges include non-linear structural dynamics due to large deformation of the flexure bearing, non-collocated and multiple sensors and actuators, multiple sources of disturbance and noise, and classical closed-loop performance tradeoffs.

Keywords: Nanopositioning System, Parallel Kinematic, Motion Control, Flexure Mechanism, Mechanical Compliance, Performance Tradeoffs

1. INTRODUCTION

A nanopositioning system is a mechatronic motion system capable of nanometric motion quality, which is defined in terms of precision (motion repeatability), accuracy (lack of error), and resolution (minimum incremental motion) (Hicks and Atherton, 1997).

While existing nanopositioning systems are capable of several hundred microns in motion range (Devasia et al., 2007), there is a growing list of applications that require a larger range (~10mm) over multiple axes (e.g. XY or XYZ). These include metrological scanning probe microscopy (Dai et al., 2004, Hausotte et al., 2005, Kramar, 2005, Sinno et al., 2007, Weckenmann and Hoffmann, 2007), scanning probe nanolithography (Salaita et al., 2007), memory storage (Sebastian et al., 2008), hard-drive and semiconductor fabrication (Van de Moosdijk et al., 2002), wafer inspection (Hongzhong et al., 2003), and imaging for stem cell research (O'Brien, 2005). In addition to large range and high motion quality, a closed-loop bandwidth of at least 100Hz is generally desirable in these applications to maintain process throughput.

Although large range nanopositioning systems based on mag-lev bearings (Kim et al., 2007, Holmes et al., 2000) and aerostatic bearings (Maeda et al., 2006, Dejima et al., 2005) have been proposed in the past, flexure bearings are attractive due to their compact size, design simplicity, zero maintenance, and potentially infinite life (Awtar, 2004). However, their main drawback is a limited motion range (Devasia et al., 2007, O'Brien, 2005). A desired motion range of ~10 mm while maintaining a motion quality ~ 1 nm represents a dynamic range of 10^7 (or 140dB) and poses challenges in terms of each of the individual physical components (flexure bearing, actuators, sensors, drivers, and micro-controller) of a flexure-based nanopositioning system. Further design challenges arise from the mechanical integration of these physical components, particularly in the case of multi-axis systems.

Our objective in this paper is to highlight these challenges and propose a physical system design based on a systematic constraint-based parallel kinematic architecture that overcomes these challenges. Moreover, while a physical system design that is 'capable' of large range and nanometric motion quality is a necessary pre-requisite; the motion quality ultimately depends on the closed-loop dynamic performance (command tracking, noise and disturbance rejection, bandwidth, and robustness). The proposed physical system design poses a set of unique controls challenges that also have to be overcome to meet the final goal of large range multi-axis nanopositioning. We identify these control system challenges and report some preliminary closed-loop testing results.

2. PHYSICAL SYSTEM DESIGN

2.1 Physical Design Challenges

A nanopositioning system is an integration of several physical components: bearing(s), actuator(s) and their drivers, sensor(s) and their drivers, and real-time microcontroller. A detailed discussion of these physical components and their pros and cons have been reported previously (Awtar and Parmar, 2010, Hubbard et al., 2006, Smith and Seugling, 2006). Here we list the most critical challenges associated with these components in achieving a large dynamic range.

Parallel kinematic flexure mechanisms: A flexure mechanism, which is a monolithic elastic structure that deforms under load to produce extremely high quality motion due to the lack of any friction and backlash (Awtar, 2004), lies at the heart of a nanopositioning system and provides motion guidance. Parallel-kinematic XY designs (Yao et al., 2007, Culpepper and Anderson, 2004, Chen et al., 2002) are well suited for multi-axis nanopositioning because of their ground-mounted actuators, thus avoiding large masses and moving cables. However, due to the lack of a systematic synthesis approach, most existing designs exhibit kinematic or geometric coupling between their motion axes leading to a restricted motion range.

Actuator and driver: Piezo-electric actuators, which have been traditionally used in nanopositioning systems, have an inherently small stroke (< 200µm). Instead, voice-coil (VC) actuators are well-suited for large-range nanopositioning, given their adequate stroke (1-10mm) along with frictionless and cog-free motion. However, their resolution relies on electrical noise (broad-band + harmonic distortions) in their current driver. Due to inherent limitations of power electronic circuits, the highest Signal to Noise and Distortion Ratio (SINAD) practically feasible is about 100dB, well below the desired 140dB. Furthermore, these VC actuators, like most linear actuators, generate motion along a specific actuation axis, and do not tolerate off-axis loads or displacements. This makes their mechanical integration with the flexure bearing challenging when large range is desired.

Sensor and sensor driver: Given their digital output, linear optical encoders are capable of large measurement ranges with nanometric resolution, circumventing the SINAD limit in analogue electronics. However, the biggest limitation of a linear encoder is that it is restricted to a specific sensing axis and does not tolerate any significant off-axis displacements. This is a problem in multi-axis nanopositioning; since end-point sensing of the moving stage is indispensable, the sensor for each axis has to be tolerant of displacements along the other axis. While capacitance probes are capable of nanometric resolution and also tolerate large off-axis displacements, they are limited in their measurement range (10-200µm). Other than interferometry, which proves to be impractical in desktop applications because of its size and setup, no single sensing method, by itself, meets the sensing requirements of large-range multi-axis nanopositioning.

Thus, it is clear that the above physical components suffer from inherent performance limitations in their ability to achieve the desired dynamic range. Additionally, for multi-axis systems, the mechanical attributes of each component (e.g. coupling between two axes in parallel-kinematic flexure bearings, fixed-axis of actuation, fixed-axis of sensing) lead to serious challenges in terms of overall system integration. To overcome these system integration challenges, it becomes essential to take into account the flexure bearing, actuators, and sensors all in conjunction in the physical system design process.

2.2 Proposed Physical System Design

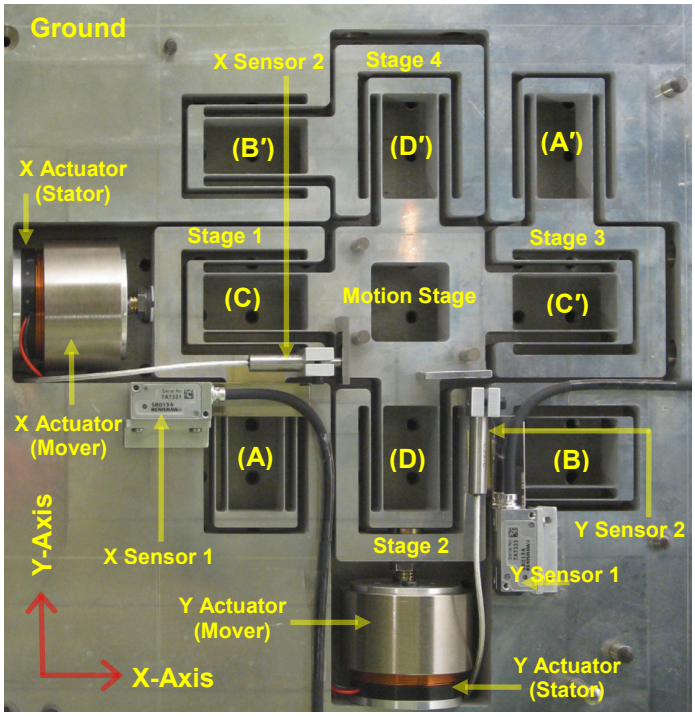

Fig.1 Large Range Parallel Kinematic (XY) Nanopositioner: Physical System Design

We propose a novel parallel kinematic physical system design, shown in Fig.1, that is generated via a systematic constraint-based design process (Awtar, 2004, Awtar and Slocum, 2007). This layout includes the flexure bearing, actuators, and sensors, and accommodates system integration challenges as described next.

The design comprises an arrangement of rigid stages interconnected by double parallelogram flexure modules (DPFM), which serve as single translational Degree of Freedom constraints. The Motion Stage is connected to Stage 1 via DPFM (C), which only allows a relative Y translation between the two. Stage 1 is connected to Ground via DPFM (A), which only allows a relative X translation between the two. Similarly, the Motion Stage is connected to Stage 3 via DPFM (C'), and Stage 3, in turn, is connected to Ground via DPFM (A'). This arrangement ensures that Stages 1 and 3 are always constrained to move along the X direction only; and, any X displacement of Stage 1 or Stage 3 is transmitted to the Motion Stage, leaving the latter free to move in the Y direction. An analogous arrangement is repeated along the Y axis.

Thus, an X force at Stage 1 produces only an X displacement of Stage 1, Stage 3 and the Motion Stage, without perturbing Stages 2 and 4. A Y force at Stage 2 produces only a Y displacement of Stage 2, Stage 4 and the Motion stage, without perturbing Stages 1 and 3. When the X and Y forces are applied simultaneously, X displacements only are produced at Stages 1 and 3; Y displacements only are produced at Stages 2 and 4; and the Motion Stage exhibits both X and Y displacements. The independence between the two axes of motion, which is a consequence of the constraint

layout and design symmetry, ensures large unconstrained motions along both axes.

Furthermore, since Stage 1 is constrained to move only in the X direction with respect to Ground due to DPFM (A), this addresses the challenge of integrating a 'fixed-axis' large-stroke X direction Voice-Coil actuator. Similarly, Stage 2 serves as the ideal location for mounting the Y direction Voice-Coil actuator. In addition to enabling X actuator integration, Stage 1 also provides an ideal location for mounting a large-stroke, fixed-axis X direction linear encoder with respect to Ground. Ideally, the X displacement of the Stage 1 should be the same as that of the Motion Stage due to DPFM (C). However, in a real implementation, some small relative X displacement between the Motion Stage and Stage 1 can be expected. This displacement is measured via a secondary X direction sensor that is required to have a small measurement range but should be tolerant to the large relative Y displacement that occurs between Stage 1 and the Motion Stage. These requirements are ideally met by a capacitance probe. Thus, the proposed physical layout enables large-range high-resolution multi-axis end-point sensing by resolving it into two simpler and practically realizable sensing tasks. A similar dual-sensor arrangement is repeated along the Y direction.

This proposed physical system design has been prototyped and tested to corroborate the above motion behaviour (Awtar and Slocum, 2007, Awtar and Parmar, 2010). The flexure bearing along with the ground frame that is used for mounting all sensors and actuators was created monolithically from a 25mm thick AL6061-T651 plate, using wire- electric discharge machining (EDM). The flexure bearing spans a 255mm x 255mm area in the centre, while the outer dimensions of the ground frame (and therefore the overall system) are 385mm x 385mm. The centre to centre distance between adjacent DPFM is 46.25mm; beam length is 47.5mm; beam in-plane thickness is 0.63mm, beam out-of-plane height is 25 mm; and, inner and outer beam spacing in each DPFM are 12.81mm and 18.44mm, respectively. The linear optical encoders used as primary sensors in both directions (RELM scale, Si-HN-4000 Read-head, and SIGNUM Interface from Renishaw) are capable of 5nm resolution, 80mm measurement range, and 135mm/s measurement speed. The encoder scales are mounted on Stages 1 and 2, while the encoder read-heads are fixed to the ground. One capacitance probe (Model # C23-C) and driver (CPL290 Elite Series) combination from Lion Precision, capable of nanometric resolution over a 50µm range at 15KHz bandwidth, is used for secondary sensing per direction. The probes is mounted on Stages 1 and 2 using a simple flexure-based clamp, while gauge blocks mounted on the Motion Stage serve as the targets. Since these capacitance probes are required to measure only the small relative X motion between the Motion Stage and Stage1, and the small relative Y motion between the Motion Stage and Stage 2, the SINAD associated with their analogue electronics does not pose a problem. Voice-coil actuators from BEI Kimco Magnetics (LA24-20-000A) that provide a force constant (K_{act}) of 11.12N/A and are capable of 111.2N bi-directional peak force are used. Since Stage 1 is constrained to move only along the X-axis w.r.t. Ground, the actuator Mover directly attached to it without the need for any additional actuator bearing. Custom built linear amplifiers comprising ultra-low noise power op-amps are employed to drive the actuators, and yield a SINAD of 90dB. Even though this does meet the desired dynamic range, we proceed with this choice keeping in mind that some degree of disturbance rejection can be achieved via feedback controls, as discussed later. A PXI-8106 real-time controller from National Instruments equipped with PXI-6289 data acquisition card was used to implement the closed-loop control algorithm.

A video of the overall experimental hardware assembly and operation may be viewed at:
www-personal.umich.edu/~awtar/hipernap

3. DYNAMIC SYSTEM MODEL

In this section, a dynamic model of the overall nanopositioning system is constructed and validated via experimental system identification, in preparation for control system design. In the frequency range of interest (*~100 Hz*), the system may be modelled as a collection of lumped springs (DPFM) and masses (rigid stages). The DPFM is modelled here as a mass-less spring along both the axial and the transverse directions as shown in Fig.2. The blue (solid) spring represents the stiffness of the DPFM in its transverse direction and the red (dotted) spring represents its stiffness in its axial direction. Even though the stiffness of the DPFM in the in-plane yaw and out-of-plane directions is of the same order as the axial stiffness, these other motions are not included in this initial modelling attempt. It is recognized that in-plane rotational and out-of-plane modes will not be captured in the resulting dynamic model, but this assumption provides a degree of simplicity and greater insight into the dynamics and controls of the proposed system.

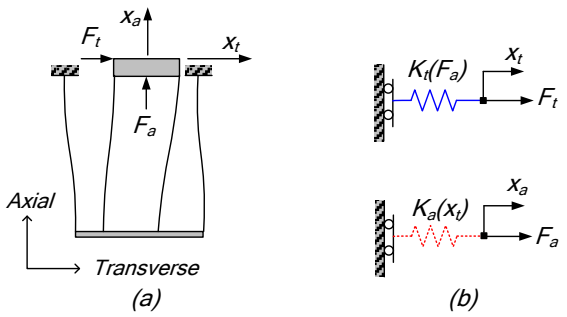

Fig.2 Lumped Spring Model of the Double Parallelogram Flexure Module (DPFM)

One of the most important consequences of large deformations in flexure mechanisms is the variation of stiffness with loads and displacements. These stiffness variations have been extensively modelled for the DPFM in the past to yield the following closed-form parametric relations (Awtar et al., 2007):

$$K_t \approx \left[12 - \frac{3}{100}\left(\frac{F_a L^2}{EI}\right)^2\right]\frac{EI}{L^3} \qquad (1)$$

$$K_a \approx \frac{1}{\left(T^2 + \frac{9}{25}x_t^2\right)} \cdot \frac{12EI}{L} \qquad (2)$$

where E is the young's modulus of the material, and L, T and I denote the length, in-plane beam thickness, and second moment of area, respectively, of the constituent beams within the DPFM. The above relations indicate that the transverse direction stiffness of the DPFM drops quadratically with the axial force (F_a), and its axial direction stiffness has an inverse-quadratic dependence on the transverse displacement (x_t).

Assuming a geometric decoupling between the two axes, a 5 Degree of Freedom (DoF) lumped parameter model for the X direction dynamics of proposed nanopositioning system is presented in Fig.3. The X displacements of the 5 rigid stages in the system define the 5-DoF. Stiffness parameter variation in the X direction model due to Y direction force and displacement is incorporated in this model by means of the above stiffness relations. An analogous model may be constructed for the Y direction of the nanopositioning system but is not presented here for the sake of brevity.

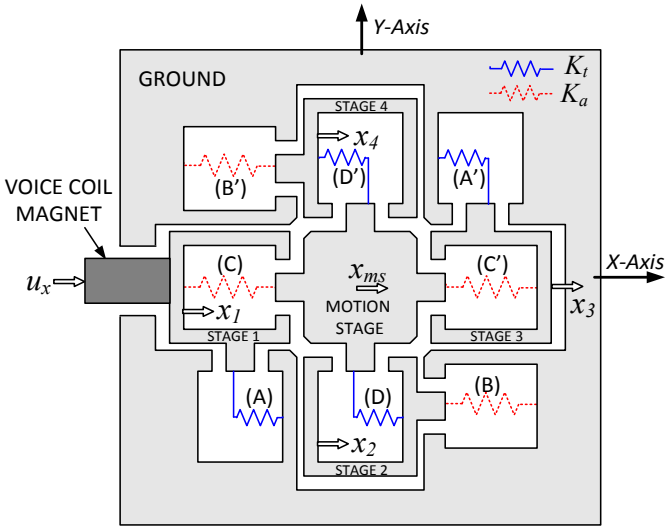

Fig.3 X-Direction Lumped Parameter Model (5-DoF)

The actuator force acting on Stage 1 along the X direction represents the system input (u_x), and the displacement of the Motion Stage along the X direction is the output (x_{ms}). The governing equation of motion for the model shown in Fig.3 can be written as follows:

$$[M]\{\ddot{x}\} + [C_d]\{\dot{x}\} + [K]\{x\} = \{f\}u_x \qquad (3)$$

where $\{x\} = [x_1\ x_2\ x_3\ x_4\ x_{ms}]^T$ and $\{f\} = [1\ 0\ 0\ 0\ 0]^T$ are 5×1 displacement and force vectors, respectively. $[M]$, $[C_d]$, and $[K]$ are all 5×5 symmetric matrices representing mass, damping, and stiffness respectively. The mass and stiffness matrices in this model are given below:

$$[M] = \begin{bmatrix} M_{is}+M_{vc} & 0 & 0 & 0 & 0 \\ 0 & M_{is} & 0 & 0 & 0 \\ 0 & 0 & M_{is} & 0 & 0 \\ 0 & 0 & 0 & M_{is} & 0 \\ 0 & 0 & 0 & 0 & M_{ms} \end{bmatrix}$$

$$[K] =$$

$$\begin{bmatrix} K_t^{(A)}+K_a^{(C)} & 0 & 0 & 0 & -K_a^{(C)} \\ 0 & K_t^{(D)}+K_a^{(B)} & 0 & 0 & -K_t^{(D)} \\ 0 & 0 & K_t^{(A')}+K_a^{(C')} & 0 & -K_a^{(C')} \\ 0 & 0 & 0 & K_t^{(D')}+K_a^{(B')} & -K_t^{(D')} \\ -K_a^{(C)} & -K_t^{(D)} & -K_a^{(C')} & -K_t^{(D')} & \begin{pmatrix} K_t^{(D)}+K_a^{(C)} \\ +K_t^{(D')}+K_a^{(C')} \end{pmatrix} \end{bmatrix}$$

where $M_{is} = 0.177\ Kg$ is the mass of Stages 1 through 4, M_{vc} = 0.570 Kg is the mass of the voice coil magnet and M_{ms} = 0.284 Kg is the mass of the Motion Stage. In the stiffness matrix, $K_t^{(A)}$ represents the transverse stiffness of the DPFM (A), and so on. These transverse and axial direction stiffness values are given by (1)-(2) for a given Y direction load or displacement.

To determine the analytical system transfer-function $G_{fx}(s) = X_{ms}(s)/U_x(s)$, a state-space model was derived using (3), with states $\{z_1\} = \{x\}$ and $\{z_2\} = \{\dot{x}\}$:

$$\begin{bmatrix} \dot{z}_1 \\ \dot{z}_2 \end{bmatrix} = \begin{bmatrix} 0 & I \\ -[M]^{-1}[K] & -[M]^{-1}[C_d] \end{bmatrix} \begin{bmatrix} z_1 \\ z_2 \end{bmatrix} + \begin{bmatrix} 0 \\ [M]^{-1} f \end{bmatrix} u_x$$
$$x_{ms} = [0\ \ 0\ \ 0\ \ 0\ \ 1\ \ 0\ \ 0\ \ 0\ \ 0\ \ 0] \begin{bmatrix} z_1 \\ z_2 \end{bmatrix} \qquad (4)$$

This analytical transfer function is plotted in Fig.4a, for the nominal X direction stiffness matrix $[K]$ when the Y actuation is zero. The first pole, which occurs at 18Hz, represents a rigid body mode in which Stage 1, Motion Stage, and Stage 3 all moves in phase with each other. The next higher mode of interest is at 1315Hz, where Motion Stage moves out of phase with respect to Stage 1, demonstrating the non-collocated sensing and actuation in our system. The corresponding pole falls outside the plotted frequency range, and is therefore not seen in Fig.4a. A similar exercise may be carried out for non-zero Y actuation, which alters the X direction stiffness matrix $[K]$ as per (1)-(2). The X direction transfer function for the case of y_{ms} = 5mm is plotted in Fig.4b. It is interesting to note that while there is no significant change in the rigid body mode, which remains at about 18Hz, the other mode mentioned above moves down from 1315Hz to 150Hz.

The above dynamic response predicted by the 5-DOF X direction model is corroborated experimentally via broadband FFT-based identification techniques using a dynamic signal analyzer (SigLab, Model 20-22A). This X direction system identification was carried out for y_{ms} values of 0 and 5mm, and the results are plotted in Figs. 4a and 4b, respectively

(solid line). The $G_{fx}(s)$ transfer functions shown here are between the actuator force and Motion Stage displacement.

The critical difference between the transfer functions in Fig. 4a and 4b is observed at 150Hz, where the phase drops below 180° for the operating point in the latter case. Since the 5-DoF model incorporates the variation in X stiffness with Y actuation, it predicts the change in pole location, and thus the early phase loss, quite accurately. The experimental transfer functions show several additional modes, very likely arising from in-plane rotational and out-of-plane dynamics, which were not included in the 5-DoF model. However, despite its simplicity, this model captures all the essential dynamics that are pertinent to Motion Stage position control, up until 150Hz, throughout the operating range of motion.

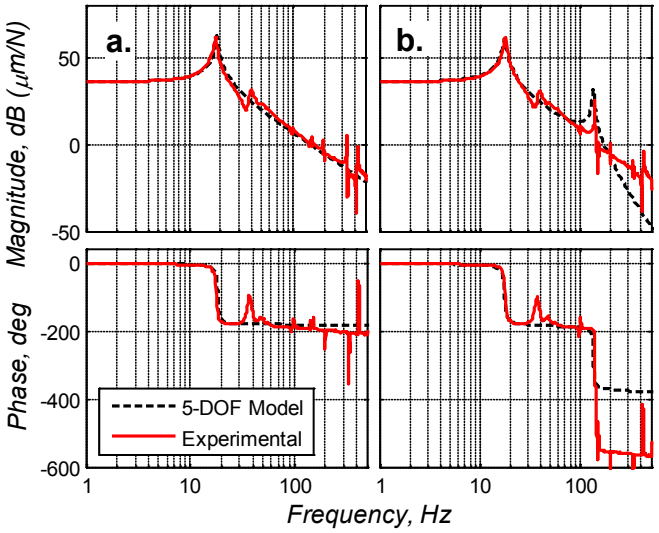

Fig.4 Comparison between Experimental and Analytical X Direction Frequency Response: (a.) y_{ms} = 0mm and (b.) y_{ms} = 5mm

4. CONTROL SYSTEM DESIGN

4.1 Control System Challenges

The performance of a nanopositioning system is specified in terms of its motion precision, accuracy, and resolution, along with speed of operation. In closed-loop operation, these specifications can be translated to equivalent control system design objectives, as follows:

1. Accuracy and precision depend on command tracking as well as low frequency noise and disturbance rejection.
2. Positioning noise and the minimum incremental motion determine the resolution. While positioning noise depends on high frequency noise and disturbance rejection, minimum incremental motion is determined by command tracking.
3. Closed-loop bandwidth determines the speed and response time of the nanopositioning system
4. Closed-loop robustness against modelling uncertainties and parameter variations affect all of the above.

In the context of the proposed physical system, several control design challenges and trade-offs are identified below in achieving the above performance objectives:

1. Most existing nanopositioning systems have a high first natural frequency because they operate over a relatively small motion range. Therefore, simple lower-order controllers with integrators (e.g., PI, PII) provide good overall performance (Devasia et al., 2007). In our case, the extended range of motion is a consequence of low primary stiffness, which also leads to a low first natural frequency (~18 Hz). In order to achieve a bandwidth greater than this first natural frequency, a higher-order controller is needed, which poses greater performance trade-offs, particularly in terms of bandwidth and noise rejection.

2. In general, lightly damped poles and zeros of in a flexible system severely affect the closed loop stability and performance (Book, 1993). In addition to this, the non-collocation of sensor and the actuator in our case leads to additional challenges in terms of achievable bandwidth (Spector and Flashner, 1990).

3. As mentioned in Section 3, the parameter variation due to coupled dynamics between the two axes, and resulting variations in the frequency response along each axis, poses further challenges in obtaining robust stability and performance.

4. Various sources of noise and disturbance in our system limit the achievable resolution. This includes feedback sensor noise, actuator driver noise, electronic noise in the data acquisition hardware, and last but not the least, mechanical floor vibrations. The individual contribution of these sources to the positioning noise will depend upon their respective magnitude, where they enter the system, the control architecture, and the controller design (Fig.5).

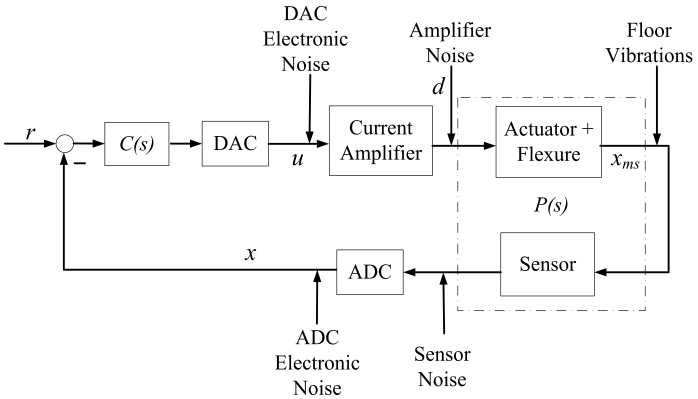

Fig.5 Control architecture implemented along each axis

4.2 Preliminary Control System Design

Although several control system objectives, challenges and limitations are identified above, here we report a preliminary control system design that can demonstrate large range nanopositioning capability at a low bandwidth. While parameter variation due to coupled dynamics has been recognized in the modelling above, its effect was found to be negligible in the low frequency range (< 150Hz). Therefore,

we propose to implement identical but independent control schemes for each axis, as shown in Fig.5. Here, the voice coil actuator, the flexure bearing, and the sensor altogether are denoted by *P(s)*, which is the same as K_{act}*$G_{fx}(s)$), assuming no sensor dynamics. The controller is represented by *C(s)*. The close-loop command is *r*, amplifier noise is *d*, actual Motion Stage displacement is x_{ms}, and measured displacement is *x*. The transfer function derived from the 5-DOF model in (4), may be stated as follows:

$$P(s) = 2.45\times10^{11}\frac{\left(s^2 + 7672s + 1.507\times10^7\right)}{\left(s^2 + 6.82s + 1.22\times10^4\right)}\times \frac{1}{\left(s^2 + 24.05s + 7.12\times10^5\right)\left(s^2 + 5491s + 7.73\times10^6\right)} \quad (5)$$

This open-loop transfer function is used design a lag-lead controller, *C(s)*, to achieve acceptable closed-loop stability and performance. The lag part includes an integrator to achieve zero steady state error and the lead part is needed to increase the phase near gain crossover frequency. In order to ensure a good roll-off at higher frequencies, an additional pole is added after the crossover frequency. Upon a few iterations, the following feedback controller was implemented:

$$C(s) = 170\frac{(s+30)(s+71)}{s(s+1150)(s+2515)} \quad (6)$$

The experimentally measured frequency response of the resulting loop transfer function *L(s) = P(s)C(s)* along with corresponding stability margins is shown in Fig.6. This confirms a Gain Margin or 12.9dB and a Phase Margin of 37.2°. Fig.7 shows the experimentally obtained frequency response of the closed loop transfer functions from *r* to *x*. The dip in gain and phase seen at lower frequencies is due to the zeros of the *C(s)*. This dip in magnitude as well as phase, albeit small, can affect command tracking when positioning accuracy is critical.

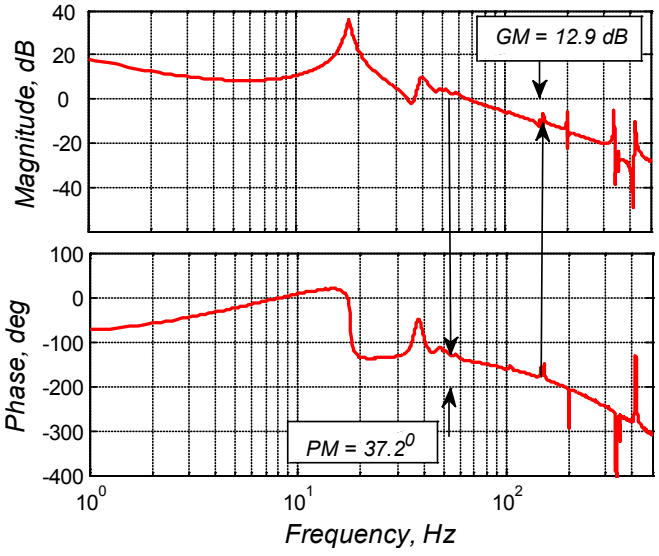

Fig.6 Experimentally Measured Frequency Response of the Loop Transfer Function, L(s)

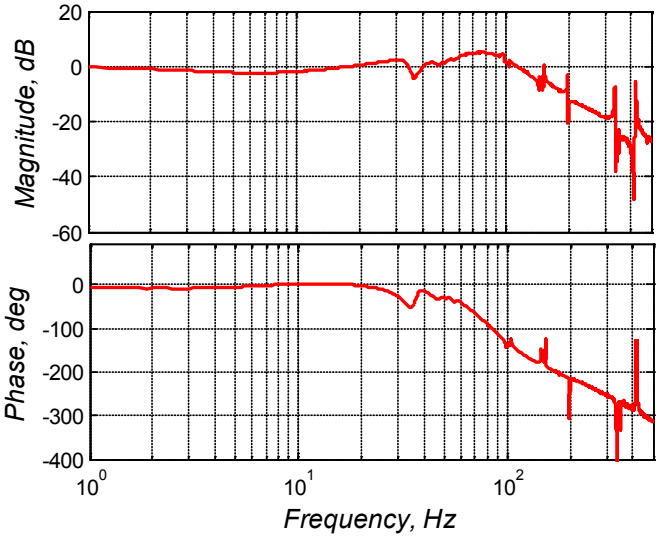

Fig. 7 Experimentally Measured Frequency Response of the Closed-loop Transfer Function

As mentioned earlier, the noise in the voice coil amplifier proves to be a major limiting factor in achieving nanometric resolution. Therefore, it is important to consider the affect of the feedback controller on the contribution of this noise to positioning resolution. The amplifier noise can be thought of as input disturbance acting on the plant, as shown in Fig.5. The closed-loop transfer function from *d* to *x* is given by:

$$T_{dx}(s) = \frac{P(s)}{1 + C(s)P(s)} \quad (7)$$

In the open-loop configuration, $T_{dx}(s)$ is simply equal to *P(s)*. Hence, the ability of the closed-loop system to reject this noise depends upon the magnitude of *C(s)*. In other words, higher the closed-loop bandwidth, which requires a high *C(s)* over a certain frequency range, also ensures improved amplifier noise rejection. However, there is obviously a limit to which *C(s)* can be increased due to concerns arising from robustness (stability margins) and sensor noise amplification.

Assuming the amplifier noise to be Gaussian white noise, its contribution is directly proportional to the area under the transfer function $T_{dx}(s)$ (Aphale et al., 2008). Fig.8 shows the comparison between the open-loop and closed-loop transfer functions *P(s)* and $T_{dx}(s)$, from *d* to *x*, for the controller given in (6). The area under the transfer function $T_{dx}(s)$ is 4 times less than the area under the transfer function *P(s)*, which qualitatively indicates a corresponding improvement in amplifier noise rejection. To measure the positioning noise, the stage was commanded to stay at a fixed position. Fig.9 shows the probability distribution of the open-loop and closed-loop positioning noise (X displacement of the Motion Stage) as measured by the sensors along X direction. The sampling frequency was fixed at 5kHz. The closed-loop positioning noise, which is also a measure of the resolution, is less than 4nm RMS. This is 3.6 times better than what is measured in the open-loop, also shown in Fig.9.

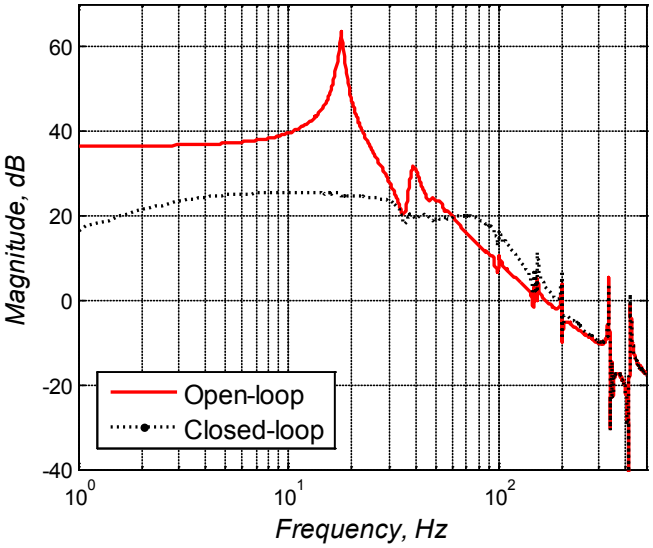

Fig.8 Experimentally Measured Transfer Function from Amplifier Noise to Motion Stage Position

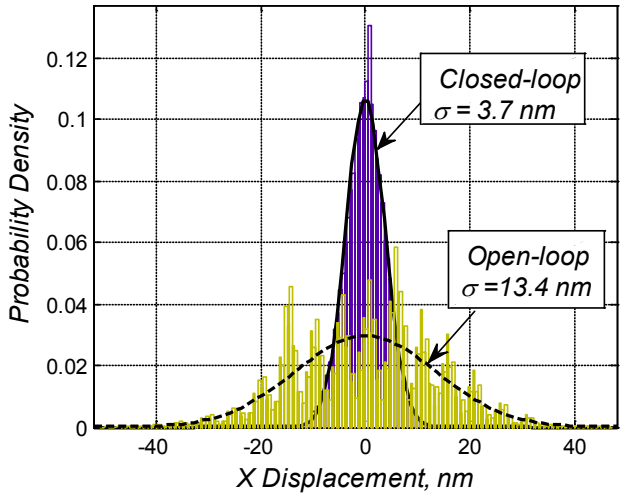

Fig.9 Amplitude Distribution of the Open-loop and Closed-loop Positioning Noise

5. PRELIMINARY CLOSED LOOP RESULTS AND DISCUSSION

In this section, we present some preliminary closed-loop performance plots for the proposed XY nanopositioning system based on the controller design discussed above. Fig.10 shows the position response of the Motion Stage to step commands of size 500µm and 20nm (inset) along the X direction, over a 3mm range. The steady state positioning resolution as seen in this time-domain plot is under 4nm RMS, in agreement with Fig.9. This figure also indicates a positioning precision and accuracy of the order of the positioning resolution. Even though the physical system is capable of motion range well above 3mm, our testing was limited due to a previously unrecognized current limit on the actuator amplifier. We are in the process of upgrading this amplifier to be able repeat this test for ranges as large as 10mm.

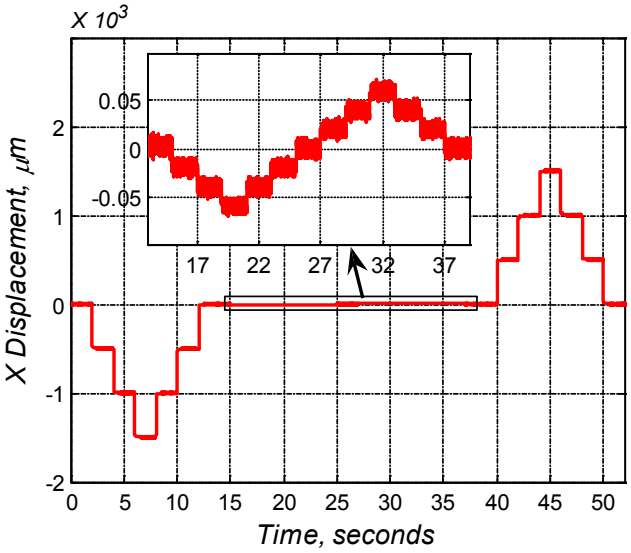

Fig.10 Motion Stage Position Response for 1mm steps and 20nm steps along X-axis

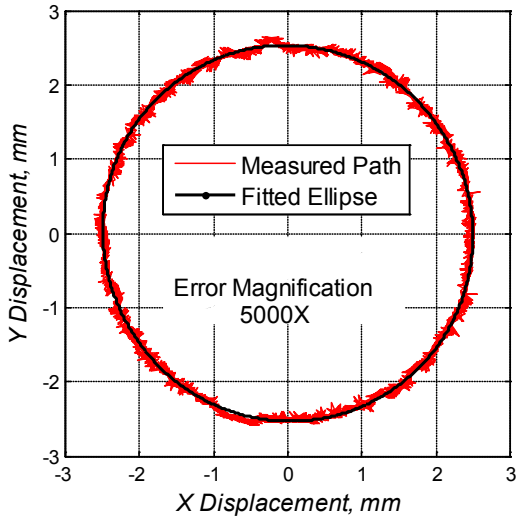

Fig.11 Motion Stage tracking a 5mm Diameter Circle; Measured Path (black), Fitted Ellipse (white)

Next, the Motion Stage was commanded to move in a 5mm diameter circle at 1Hz. This was done by sending sinusoidal reference commands along both the axes with a magnitude of 2.5mm and separated in phase by 900. An unanticipated large deviation of the actual path of the Motion Stage from the reference circle was observed. A least square ellipse was fitted to the actual path reveals a maximum trajectory deviation of approximately 2.25µm. The positioning noise with respect to the fitted ellipse was measured to be less than 12nm RMS. Fig.11 shows the measured position response of the Motion Stage along with the least square fit ellipse. For better visualization, the error from the least square fit ellipse is magnified 5000 times.

Even though the positioning noise and therefore resolution (12nm RMS) is reasonable, the trajectory tracking error (or lack of positioning accuracy) is considerably large, especially when compared to the above single axis positioning results.

This error is a consequence of the fact that over a motion range of several millimetres, even a small difference in the actual phase of the two axes leads to a pronounced deviation from the command trajectory. One of the reasons why command tracking in the two-axis control case suffers is a reduction in the controller gain to avoid an unexpected instability. We believe that this instability, not seen in the single-axis case, arises from a cross-axis coupling dynamics that was ignored in the modelling and controller design. Our on-going research efforts include characterizing this non-linear cross-axis coupling, exploring methods for suppressing it, and developing feed-forward and feedback control schemes to provide the desired controls performance despite this unusual dynamic behaviour.

REFERENCES

Aphale, S. S., Bhikkaji, B. & Moheimani, S. O. R. (2008) Minimizing scanning errors in piezoelectric stack-actuated nanopositioning platforms. *IEEE Transactions on Nanotechnology,* 7**,** 79-90.

Awtar, S. (2004) Analysis and Synthesis of Planer Kinematic XY Mechanisms. Cambridge MA, Massachusetts Institute of Technology.

Awtar, S. & Parmar, G. (2010) Design of a Large Range XY Nanopositioning System. *ASME IDETC & CIE.* Montreal Canada.

Awtar, S. & Slocum, A. H. (2007) Constraint-based Design of Parallel Kinematic XY Flexure Mechanisms. *ASME Journal of Mechanical Design,* 129**,** 816-830.

Awtar, S., Slocum, A. H. & Sevincer, E. (2007) Characteristics of Beam-based Flexure Modules. *ASME Journal of Mechanical Design,* 129**,** 625-639.

Book, W. J. (1993) Controlled motion in an elastic world. *Transactions of the ASME. Journal of Dynamic Systems, Measurement and Control,* 115**,** 252-61.

Chen, K. S., Trumper, D. L. & Smith, S. T. (2002) Design and control for an electromagnetically driven X-Y-[theta] stage. *Precision Engineering,* 26**,** 355-369.

Culpepper, M. L. & Anderson, G. (2004) Design of a low-cost nano-manipulator which utilizes a monolithic, spatial compliant mechanism. *Precision Engineering,* 28**,** 469-482.

Dai, G., Pohlenz, F., Danzebrink, H.-U., Xu, M., Hasche, K. & Wilkening, G. (2004) Metrological large range scanning probe microscope. *Review of Scientific Instruments,* 75**,** 962-969.

Dejima, S., Gao, W., Katakura, K., Kiyono, S. & Tomita, Y. (2005) Dynamic modeling, controller design and experimental validation of a planar motion stage for precision positioning. *Precision Engineering,* 29**,** 263-271.

Devasia, S., Eleftheriou, E. & Moheimani, S. O. R. (2007) A Survey of Control Issues in Nanopositioning. *IEEE Transactions on Control Systems Technology,* 15**,** 802-23.

Hausotte, T., Jaeger, G., Manske, E., Hofmann, N. & Dorozhovets, N. (2005) Application of a Positioning and Measuring Machine for Metrological Long-range Scanning Force Microscopy. *SPIE.* 1 ed. San Diego, CA.

Hicks, T. R. & Atherton, P. D. (1997) *The Nanopositioning Book*, Queensgate Instruments Ltd.

Holmes, M., Hocken, R. & Trumper, D. (2000) The long-range scanning stage: a novel platform for scanned-probe microscopy. *Precision Engineering,* 24**,** 191-209.

Hongzhong, L., Bingheng, L., Yucheng, D., Yiping, T. & Dichen, L. (2003) A motor-piezo actuator for nano-scale positioning based on dual servo loop and nonlinearity compensation. *Journal of Micromechanics and Microengineering,* 13**,** 295-9.

Hubbard, N. B., Culpepper, M. L. & Howell, L. L. (2006) Actuators for micropositioners and nanopositioners. *Applied Mechanics Reviews,* 59**,** 324-334.

Kim, W.-J., Verma, S. & Shakir, H. (2007) Design and precision construction of novel magnetic-levitation-based multi-axis nanoscale positioning systems. *Precision Engineering,* 31**,** 337-350.

Kramar, J. A. (2005) Nanometre Resolution Metrology with the Molecular Measuring Machine. *Measurement Science & Technology,* 16**,** 2121-28.

Maeda, G. J., Sato, K., Hashizume, H. & Shinshi, T. (2006) Control of an XY nano-positioning table for a compact nano-machine tool. *JSME International Journal, Series C (Mechanical Systems, Machine Elements and Manufacturing),* 49**,** 21-7.

O'brien, W. (2005) Long-range motion with nanometer precision. *Photonics Spectra.* Laurin Publishing Co. Inc., Pittsfield, MA 01202-4949, United States.

Salaita, K., Wang, Y. H. & Mirkin, C. A. (2007) Applications of Dip-Pen Nanolithography. *Nature Nanotechnology,* 2**,** 145-55.

Sebastian, A., Pantazi, A., Pozidis, H. & Eleftheriou, E. (2008) Nanopositioning for probe-based data storage [Applications of Control]. *IEEE Control Systems Magazine,* 28**,** 26-35.

Sinno, A., Ruaux, P., Chassagne, L., Topcu, S. & Alayli, Y. (2007) Enlarged Atomic Force Microscopy Scanning Scope: Novel Sample-holder Device with Millimeter Range. *Review of Scientific Instruments,* 78**,** 1-7.

Smith, S. T. & Seugling, R. M. (2006) Sensor and actuator considerations for precision, small machines. *Precision Engineering,* 30**,** 245-264.

Spector, V. A. & Flashner, H. (1990) Modeling and design implications of noncollocated control in flexible systems. *Transactions of the ASME. Journal of Dynamic Systems, Measurement and Control,* 112**,** 186-93.

Van De Moosdijk, M., Van Den Brink, E., Simon, K., Friz, A., Phillipps, G., Travers, R. & Raaymakers, E. (2002) Collinearity and stitching performance on an ASML stepper. *SPIE.* Santa Clara, CA, SPIE-Int. Soc. Opt. Eng.

Weckenmann, A. & Hoffmann, J. (2007) Long Range 3 D Scanning Tunnelling Microscopy. *CIRP Annals - Manufacturing Technology,* 56**,** 525-528.

Yao, Q., Dong, J. & Ferreira, P. M. (2007) Design, analysis, fabrication and testing of a parallel-kinematic micropositioning XY stage. *International Journal of Machine Tools and Manufacture,* 47**,** 946-961.